

MOLECULAR GAS DYNAMICS OF THE LENSED WET-MERGER RXSJ1131-1231 AT Z=0.654

T. K. DAISY LEUNG AND DOMINIK A. RIECHERS

Department of Astronomy, Space Sciences Building, Cornell University, Ithaca, NY 14853, USA; tleung@astro.cornell.edu

To be submitted to the ApJ

ABSTRACT

We CO($J = 2 \rightarrow 1$) observations with the Plateau de Bure Interferometer. evidence for differential lensing. wet-merger, Dynamical lens modeling the intrinsic dynamics and blah are suggestive of a rotating disk morphology, consistent with previous results based on optical observations.

Subject headings: ISM: molecular – infrared: galaxies – galaxies: mergers – galaxies: starburst – galaxies: evolution

1. INTRODUCTION

In this paper, we explore the ISM properties of the quadruply imaged quasar RXS J113151.62-123158 (hereafter RXJ1131) at $z_{\text{AGN}} = 0.685$, with an Einstein ring of size $1''.83$ in radius. The foreground lensing galaxy is an elliptical galaxy at $z_L = 0.295$. The redshifts are spectroscopically confirmed by [Sluse et al. \(2003\)](#). A black hole mass estimate of $M_{\text{BH}} < 2 \times 10^8 M_\odot$ is also reported based on X-ray observations ([Reis et al. 2014](#)).

This paper is structured as follows. In §2 and §3, we outline the details of the observations and data reduction process. In §4, we report the measurements of the CO lines and photometry from optical to radio wavelengths. In §5, we represent our dynamical lens modeling on the CO($J = 2 \rightarrow 1$) data and the physical properties inferred for RXJ1131. In §6, we discuss the results and implications of this study in the context of molecular gas evolution in mergers and massive galaxies. Finally, we summarize the main results of this study and present our conclusions in §7. We use a concordance Λ CDM cosmology throughout this paper, with parameters from the WMAP9 results: $H_0 = 69.32 \text{ km s}^{-1} \text{ Mpc}^{-1}$, $\Omega_M = 0.29$, and $\Omega_\Lambda = 0.71$ ([Hinshaw et al. 2013](#)).

2. OBSERVATIONS

2.1. PdBI CO($J = 2 \rightarrow 1$)

Observations of the CO($J = 2 \rightarrow 1$) rotational line ($\nu_{\text{rest}} = 230.5379938 \text{ GHz}$; $\nu_{\text{obs}} = 139.4 \text{ GHz}$) toward the gravitationally lensed galaxy RXJ1131-1231 at $z_{\text{QSO}} = 0.658$ were carried out using IRAM Plateau de Bure Interferometer (PdBI; Program ID: S14BX001; PI: D. Riechers). Two observing runs were carried out on 2014 December 06 and 2015 February 05 under good weather conditions in the C and D array configurations, respectively. The 2 mm receivers were used to cover the redshifted CO($J = 2 \rightarrow 1$) line and the underlying continuum emission, employing a correlator setup providing an effective bandwidth of 3.6 GHz and a spectral resolution of 10.0 MHz ($\sim 21.5 \text{ km s}^{-1}$). This resulted in 3.75 hours of cumulative six antenna-equivalent on-source time after discarding unusable visibility data. The nearby quasars 1127-145 and 1124-186 were observed every 22 minutes for pointing, secondary amplitude, and phase

calibration, and 1055+018 was observed as the bandpass calibrator for both tracks. MWC349 and 3C279 were observed as primary flux calibrators for the C and D array observations, respectively, yielding $\lesssim 15\%$ calibration accuracy.

The GILDAS package was used to reduce and analyze the visibility data which are then imaged and deconvolved using the CLEAN algorithm with “natural” weighting. This yields a synthesized clean beam size of $4''.44 \times 1''.95$ (PA = 13°). The final rms noise is $\sigma = 1.45 \text{ mJy km s}^{-1} \text{ beam}^{-1}$ over 10 MHz (21.5 km s^{-1}). The continuum image at $\nu_{\text{cont}} \sim 139 \text{ GHz}$ is created by averaging over all the 3.16 GHz line-free channels. This yields an rms noise of $0.082 \text{ mJy beam}^{-1}$.

2.2. CARMA CO($J = 3 \rightarrow 2$)

Observations of the CO($J = 3 \rightarrow 2$) rotational line in RXJ1131 ($\nu_{\text{rest}} = 345.7959899 \text{ GHz}$; $\nu_{\text{rest}} = 209.1 \text{ GHz}$) were carried out with the Combined Array for Research in Millimeter-wave Astronomy (CARMA; Program ID: cf0098; PI: D. Riechers) in the D array configuration on 2014 February 02 under poor 1.5 mm weather conditions and on 2014 February 17 under good 1.5 mm weather conditions. The correlator setup provides a bandwidth of 3.75 GHz in each sideband and a spectral resolution of 12.5 MHz ($\sim 17.9 \text{ km s}^{-1}$). The line was placed in the lower sideband with the local oscillator tuned to $\nu_{\text{LO}} \sim 216 \text{ GHz}$. The radio quasars J1127-189 (first track) and 3C273 (second track) were observed every 15 minutes for pointing, amplitude, and phase calibration. Mars was observed as the primary absolute flux calibrator and 3C279 was observed as the bandpass calibrator for both tracks. This results in a total on-source time of 2.94 hours after flagging poor visibility data.

Given that the phase calibrator used for the first track was faint and was observed under poor weather conditions and that the phase calibrator used for the second track was far from our target source, the phase calibration is subpar, with an rms scatter $\sim 60^\circ$ over $\sim 135 \text{ m}$. We thus conservatively estimate a calibration accuracy of $\sim 45\%$ based on the flux scale uncertainties, the gain variations over time, and the phase scatter on the calibrated data. We therefore treat its line intensity with caution and ensure that any

physical interpretation of this system does not rely on this quantity.

The MIRIAD package was used to calibrate the visibility data which are then imaged and deconvolved using the CLEAN algorithm with “natural” weighting. This yields a synthesized clean beam size of $3''.2 \times 1''.9$ (PA = 8°) for the lower sideband image cube. The final rms noise is $\sigma = 13.3 \text{ mJy km s}^{-1} \text{ beam}^{-1}$ over a channel width of 25 MHz. An rms noise of $\sigma = 0.83 \text{ mJy beam}^{-1}$ is reached by averaging over the line-free channels.

2.3. VLA (Archival)

Our analysis also uses archival data of the 5 GHz radio continuum obtained with the Very Large Array (VLA; Program ID: AW741; PI: Wucknitz). Observations were carried out on 2008 December 29 under excellent weather conditions in the A array configurations for a total of ~ 7 hours on-source time. The C-band receivers were used with a continuum mode setup, providing a bandwidth of 50 MHz in each sideband. The nearby radio quasar 1130–149 was observed every 10 minutes for pointing, amplitude, and phase calibration, 1331–305 was observed as the primary flux calibrator, and 0319+415 was observed as the bandpass calibrator, yielding $\sim 10\%$ calibration accuracy. We use AIPS to calibrate the visibility data which are then imaged and deconvolved using the CLEAN algorithm using robust=0. This yields a synthesized clean beam size of $0''.49 \times 0''.35$ (PA = $0''.18$) and a final rms noise of $\sigma = 13 \text{ } \mu\text{Jy beam}^{-1}$.

3. HST ASTROMETRY

We obtained an *HST* image taken with the F555W filter (V-band) using the ACS/Wide Field Camera from the Hubble Legacy Archive¹ with a goal to understand the origin of the emission detected in our mm observations. The details of the observations can be found in C06. We adopt the VLA 5 GHz map of $\sim 0''.5$ resolution as the reference coordinate frame to align the optical (V-band) image. We shift the latter to the east by $0''.5963$ in R.A. and $+0''.8372$ in Dec., which is consistent with the typical astrometric precision ($1''$ – $2''$) of images from the Hubble Legacy Archive². This astrometric correction is critical to avoid artificial spatial offsets between different emitting regions and to carry out our lens modeling, in which the absolute position of the foreground lensing galaxy is guided by its coordinates in the optical image, where its emission is clearly detected. The VLA image is calibrated using a well-monitored phase calibrator, with absolute positional accuracy of $\sim 2 \text{ mas}$. For this reason, the absolute alignment between the VLA image and other interferometric images reported in this paper are expected to have astrometric precision better than $0''.1$, modulo uncertainties related to the SNR, phase errors, and beam size.

¹ Based on observations made with the NASA/ESA Hubble Space Telescope, and obtained from the Hubble Legacy Archive, which is a collaboration between the Space Telescope Science Institute (STScI/NASA), the Space Telescope European Coordinating Facility (ST-ECF/ESA) and the Canadian Astronomy Data Centre (CADC/NRC/CSA).

² http://hla.stsci.edu/hla_faq.html

4. RESULTS

4.1. CO($J = 2 \rightarrow 1$) Emission

We detected the CO($J = 2 \rightarrow 1$) line emission toward the background galaxies at $\gtrsim 27\sigma$ significance, confirming the redshift at $z_{\text{CO}} = 0.65370 \pm 0.0005$. The emission is spatially and dynamically resolved with a highly asymmetric double-horned line profile as shown in Figure 1. Fitting a double Gaussian results in peak flux densities of 75.3 ± 2.6 and $24.0 \pm 2.0 \text{ mJy}$, and a FWHM of $179 \pm 9 \text{ km s}^{-1}$ and $255 \pm 28 \text{ km s}^{-1}$, respectively. The peaks are separated by $\Delta v_{\text{sep}} = 400 \pm 12 \text{ km s}^{-1}$. The total integrated line flux is $24.1 \pm 2.3 \text{ Jy km s}^{-1}$.

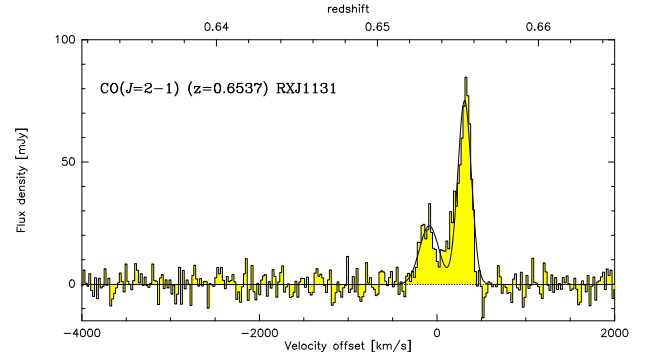


FIG. 1.— Spectrum of CO($J = 2 \rightarrow 1$) emission toward RXJ1131. The velocity scale is with respect to $z=0.6537$, which is approximately the line center considering the asymmetry as a result of differential lensing. A detailed discussion of this effect is presented in §5.1.2 and the magnification factors for various kinematic components are listed in Table 3.

We construct the zeroth moment map (Figure 2) and the higher-order first and second moment maps (Figure 8) using the uv -continuum subtracted data cube over a velocity range of $\Delta v \sim 750 \text{ km s}^{-1}$. The higher-order moment maps are created using channel maps with 3σ clipping. The peak flux density is $8.12 \pm 0.30 \text{ Jy km s}^{-1} \text{ beam}^{-1}$ in the intensity-integrated map. The deconvolved source size FWHM is estimated to be $5''.1 \pm 0''.72 \times 3''.72 \pm 0''.66$, and thus, the emission is resolved over ~ 2.2 beams. While the lensed emission is not strictly distributed as two-dimensional Gaussian; the fit recovers the line intensity enclosed by the emitting region, we therefore take this as an estimate on the extent of the lensed emission. On the other hand, if we assume the spatial distribution of the lensed molecular gas emission is similar to that in the optical to near-IR wavelengths, the lensed emission would be more accurately described by an annulus, enclosing the partially complete “Einstein Ring” and the lensed knots (see Figure 2).

We also place an upper limit on HNC($J = 2 \rightarrow 1$) line emission in the foreground galaxy at $z \sim 0.295$. Assuming a typical line width of 300 km s^{-1} , this corresponds to a 3σ limit of $0.35 \text{ mJy km s}^{-1} \text{ beam}^{-1}$.

4.2. CO($J = 3 \rightarrow 2$) Emission

We detect CO($J = 3 \rightarrow 2$) line emission toward RXJ1131 at 3.5σ significance. The spectrum is shown in Figure 3, which seems to have a double-peak profile. This is expected if RXJ1131 is truly a disk galaxy (see previous

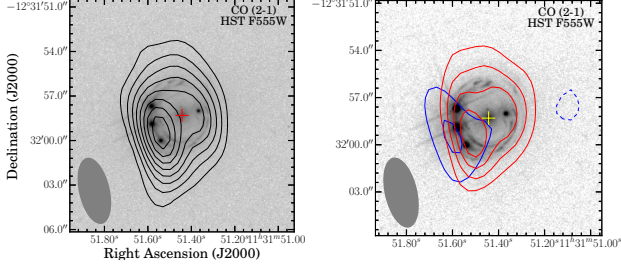


FIG. 2.— Left: an overlay of the velocity-integrated CO($J=2 \rightarrow 1$) emission on the *HST* V-band (F555W) image. Right: contours are color-coded to represent the red and blue wings of the emission. The contours start at 3σ and increment at steps of $\pm 3\sigma$, where $\sigma = 0.3 \text{ mJy beam}^{-1}$. The crosses denote the location of the foreground galaxy at $z=0.295$.

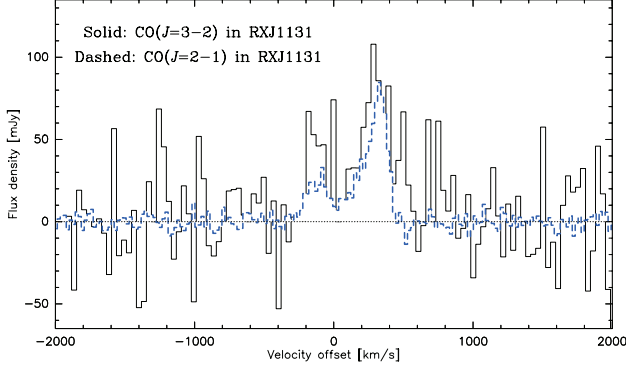


FIG. 3.— CARMA CO($J=3 \rightarrow 2$) line profile (solid) without continuum subtraction is over-plotted on the continuum-subtracted PdBI CO($J=2 \rightarrow 1$) line profile (dashed). The velocity scale is with respect to $z=0.6537$, which corresponds to the dynamical center of the CO($J=2 \rightarrow 1$) line. The spectral resolution for CO($J=3 \rightarrow 2$) and CO($J=2 \rightarrow 1$) is 35.8 km s^{-1} and 21.5 km s^{-1} , respectively.

sections). The high phase noise in the calibration leads to a low SNR detection. We thus estimate the line intensity to be $35.7 \pm 21.9 \text{ Jy km s}^{-1}$ by summing up fluxes over the FWZI linewidth used to infer CO($J=2 \rightarrow 1$) line intensity ($\sim 700 \text{ km s}^{-1}$).

Assuming the spatial extents between CO($J=2 \rightarrow 1$) and CO($J=3 \rightarrow 2$) are similar and therefore magnified by the same amount, the line intensities correspond to a brightness temperature ratio of $r_{32} = T_{\text{CO}(J=3 \rightarrow 2)} / T_{\text{CO}(J=2 \rightarrow 1)} = 0.66 \pm 0.41$.

4.3. Continuum Emission

No 1.5 mm continuum emission is detected at the position of CO($J=3 \rightarrow 2$) down to a 3σ limit of $2.49 \text{ mJy beam}^{-1}$. This is consistent with the spectrum shown in Figure 3.

We detect PdBI 2 mm continuum in Figure 4. The integrated flux density is $1.2 \pm 0.2 \text{ mJy}$, with a peak flux $S_\nu = 800 \pm 88 \mu\text{Jy beam}^{-1}$ centering on the lensing galaxy. Slightly extended emission is also detected along the lensed arc. This suggests that the detected emission comes from both the foreground galaxy and the background galaxy and that the emission is marginally resolved along its major axis. We subtract a point source model in uv -plane to remove the unresolved emission toward the foreground galaxy. The peak flux ($0.39 \pm 0.08 \text{ mJy}$) in the residual map coincides with the lensed arc, and is con-

sistent with the difference between the integrated and the peak flux in the original continuum map ($\sim 0.4 \text{ mJy}$). We therefore adopt $S_\nu = 0.39 \pm 0.08 \text{ mJy}$ as the 2 mm continuum emission toward the background galaxy.

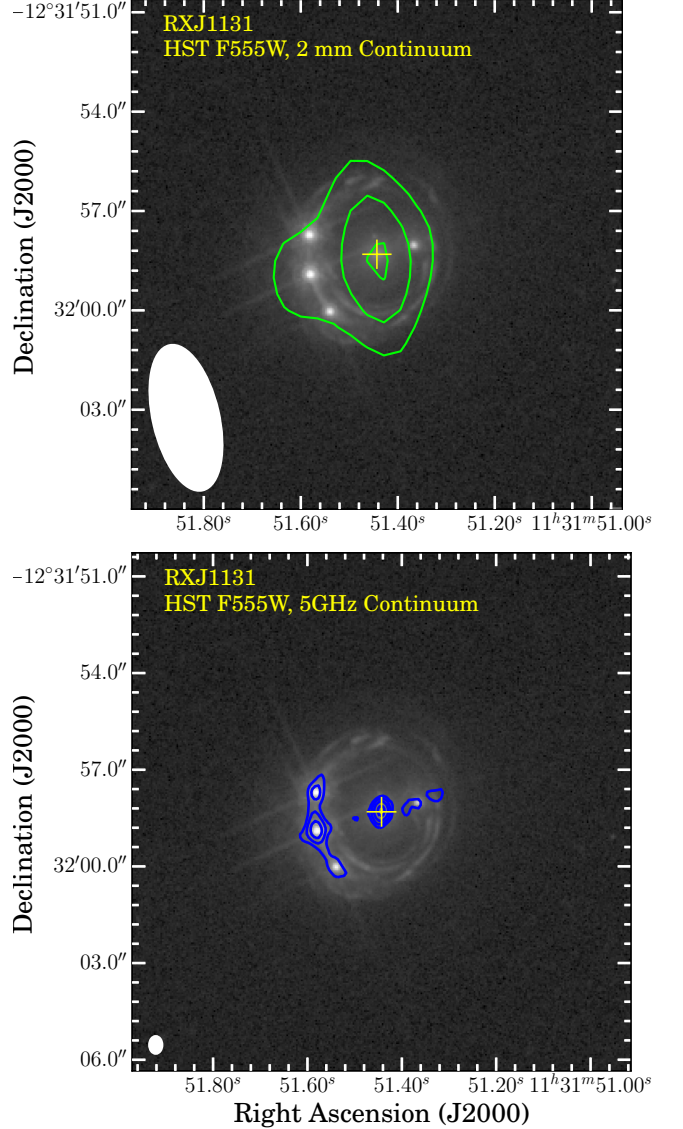


FIG. 4.— Top: an overlay of the 2 mm continuum emission on the optical image. Bottom: VLA 5 GHz continuum emission is overlaid on the optical image. Contours in both images start and increment at steps of $\pm 3\sigma$, where $\sigma_{2\text{mm}} = 0.082 \text{ mJy beam}^{-1}$ and $\sigma_{5\text{GHz}} = 13 \mu\text{Jy beam}^{-1}$ in the left and right panel, respectively. The central crosses indicate the centroid of the foreground galaxy, as detected in the optical image. The synthesis beams are shown in the bottom left corner of each panel.

The VLA C-band continuum image in Figure 4 shows resolved emission from the jets and core of the foreground elliptical galaxy as well as emission toward the background quasar. Multiple peaks are seen along the arc and their centroids coincide with the optical emission from the quasar. We extract the flux densities for the arc and the core in Table 1. We find a spectral index of $\alpha_{6\text{cm}}^{2\text{mm}} = -0.024$ for the foreground galaxy and $\alpha_{6\text{cm}}^{2\text{mm}} = -0.345$ for the background galaxy by fitting a power-law ($S_\nu \propto \nu^\alpha$) to the con-

tinuum emission at 5 GHz and 2 mm.

4.4. Photometry

We compile mid-IR (MIR) to far-IR broadband photometry from various catalogs available on the NASA/IPAC Infrared Science Archive (IRSA) in Table 1 with aperture corrections when warranted. These data were obtained from the Two Micron All Sky Survey (2MASS; [Skrutskie et al. 2006](#)), the Wide-field Infrared Survey Explorer (WISE; [Wright et al. 2010](#)), the *Infrared Astronomical Satellite* (IRAS; [Neugebauer et al. 1984](#)), and the Multi-band Imaging Photometer (MIPS; [Rieke et al. 2004](#)) and Mid-infrared Infrared Array Camera (IRAC; [Fazio et al. 2004](#)) on the *Spitzer Space Telescope*. We retrieve PBCD (level 2) *Spitzer*/IRAC images from the Spitzer Heritage Archive and perform aperture photometry on the channel 1 image to extract the flux density at $3.6\ \mu\text{m}$ since it is not available from the IRSA archive.

The emission in the IRAC images is slightly extended. We thus use the *HST* image ($\sim 0.''07$ resolution) to determine origins of their centroids, all of which are found to be centered at the position corresponding to the lensed emission from the background galaxy. To recover the diffuse background emission, we subtract a point source model centered on the lensing galaxy, using the average FWHM found by fitting a Gaussian profile to several field stars with the IMEXAM routine of IRAF. We perform aperture photometry on the residual image to obtain decomposed flux measurements from the background galaxy. The photometry for the foreground galaxy is then obtained by subtracting the background emission from the observed total flux. The resulting photometry in Table 1 are obtained after performing an aperture correction described in the IRAC Instrument Handbook³ to correct for the fact that the imaging was calibrated using a $12''$ aperture, which is larger than the aperture ($5.''8$) we used to perform aperture photometry.

We fit a power-law spectrum to the decomposed IRAC photometry to disentangle the observed total flux at MIPS $24\ \mu\text{m}$ into the foreground and background galaxies. We find a spectral index of $\alpha \sim -1.8$ and $\alpha \sim -0.85$ for the lensing galaxy and RXJ1131, respectively. This is consistent with the mean $3.6\text{--}8\ \mu\text{m}$ spectral slope of $\alpha = -1.07 \pm 0.53$ found for unobscured AGN ([Stern et al. 2005](#)). An extrapolation of the fit to $24\ \mu\text{m}$ yields $33.96 \pm 0.01\ \text{mJy}$ and $25.19 \pm 0.03\ \text{mJy}$ for the foreground galaxy and RXJ1131, respectively. We note that the IRAC photometry includes emission from old stellar populations and is prone to dust extinction. Hence, the decomposed fluxes are only our best estimate of the warm dust emission. We incorporate the decomposed $24\ \mu\text{m}$ point in our SED fitting to provide some constraints on the Wien tail beyond the dust peak of the spectral energy distribution (SED) of RXJ1131. Details of the SED modeling is presented in §5.4.

Extraction of the *Herschel*/SPIRE photometry was carried out using SUSSEXTRACTOR within the *Herschel* In-

TABLE 1
PHOTOMETRY DATA

Wavelength μm	Frequency GHz	Flux Density mJy	Instrument
0.555	540167	0.056 ± 0.006	<i>HST</i> -ACS/V-Band (L)
0.555	540167	0.009 ± 0.0041	<i>HST</i> -ACS/V-Band (H)
0.814	368295	0.238 ± 0.013	<i>HST</i> -ACS/I-Band (L)
0.814	368295	0.041 ± 0.0054	<i>HST</i> -ACS/I-Band (H)
1.25	239834	1.009 ± 0.09	2MASS/J-Band
1.6	187370	0.539 ± 0.041	<i>HST</i> -NICMOS(NIC2)/H-Band (L)
1.6	187370	0.133 ± 0.004	<i>HST</i> -NICMOS(NIC2)/H-Band (H)
1.65	181692	1.448 ± 0.12	2MASS/H-Band
2.17	138153	2.064 ± 0.16	2MASS/Ks-Band
3.4	88174.2	7.027 ± 0.14	WISE/W1
3.6	83275.7	5.618 ± 0.0021	<i>Spitzer</i> /IRAC
3.6	83275.7	5.034 ± 0.0021	<i>Spitzer</i> /IRAC (H)
3.6	83275.7	0.585 ± 0.003^a	<i>Spitzer</i> /IRAC
4.5	66620.5	7.803 ± 0.0021	<i>Spitzer</i> /IRAC
4.5	66620.5	6.009 ± 0.0017	<i>Spitzer</i> /IRAC (H)
4.5	66620.5	1.794 ± 0.0027^a	<i>Spitzer</i> /IRAC
4.6	65172.3	8.872 ± 0.16	WISE/W2
5.8	51688.4	10.720 ± 0.0051	<i>Spitzer</i> /IRAC
5.8	51688.4	7.557 ± 0.003	<i>Spitzer</i> /IRAC (H)
5.8	51688.4	3.163 ± 0.0059^a	<i>Spitzer</i> /IRAC
8.0	37474.1	14.470 ± 0.0041	<i>Spitzer</i> /IRAC
8.0	37474.1	9.881 ± 0.0039	<i>Spitzer</i> /IRAC (H)
8.0	37474.1	4.589 ± 0.0057^a	<i>Spitzer</i> /IRAC
12	24982.7	21.960 ± 0.42	WISE/W3
12	24982.7	< 400	IRAS
22	13626.9	55.110 ± 1.9	WISE/W4
24	12491.4	70.204 ± 0.026	<i>Spitzer</i> /MIPS
25	11991.7	< 500	IRAS
60	4996.54	< 600	IRAS
100	2997.92	< 1000	IRAS
250	1199.17	289.4 ± 9.6	<i>Herschel</i> /SPIRE
350	856.55	168.2 ± 8.6	<i>Herschel</i> /SPIRE
500	599.585	56.8 ± 8.8	<i>Herschel</i> /SPIRE
1387.93	216	< 2.492	CARMA
2152.82	139.256	1.230 ± 0.220	PdBI (integrated)
2152.82	139.256	0.799 ± 0.082	PdBI (peak)
2152.82	139.256	0.400 ± 0.082^b	PdBI
61414	4.8815	1.273 ± 0.042	VLA/Cband (arc)
61414	4.8815	0.866 ± 0.027	VLA/Cband (core)

REFERENCES. — The *HST* photometry is taken from C06.

NOTE. — (H) and (L) in column 4 indicate the flux (in column 3) of RXJ1131 and its lensing galaxy, respectively. The IRAC photometry at $3.6\ \mu\text{m}$ is extracted directly from the image and from the *Spitzer* Heritage Archive for channels 2–4 ($4.5\ \mu\text{m}$, $5.8\ \mu\text{m}$, and $8.0\ \mu\text{m}$). The upper limits are the 3σ limits.

^a Flux obtained by subtracting the emission of RXJ1131 from the total emission within an aperture.

^b Flux extracted from the residual map after subtracting a point-source model.

terative Processing Environment (HIPE; [Ott 2010](#)) on Level 2 maps obtained from the *Herschel* Science Archive. These maps were processed by the SPIRE pipeline version 13.0 within HIPE. The SUSSEXTRACTOR task estimates the flux density from an image convolved with a kernel derived from the SPIRE beam. The flux density measured by SUSSEXTRACTOR is additionally confirmed using the Timeline Fitter, which performs photometry by fitting a 2D elliptical Gaussian to the Level 1 data at the source position given by the output of SUSSEXTRACTOR. The fluxes obtained from both methods are consistent within the uncertainties.

5. ANALYSIS

5.1. Lens modeling

At the angular resolution of the CO($J=2 \rightarrow 1$) data, the images are resolved over ~ 2 resolution elements. Given the extent of the lensed emission, this implies that our

³ <http://irsa.ipac.caltech.edu/data/SPITZER/docs/irac/iracinstrumenthandbook/>

CO($J=2 \rightarrow 1$) observations do not resolve structures (e.g. knots and arcs) of the lensed emission (i.e., sub-optimal for performing lens modeling). Nevertheless, the high spectral resolution of this data provides dynamical information on spatial scales smaller than the beam (see Figure 8). Hence, with the high SNR, we reconstruct the intrinsic gas dynamics by carrying out a parametric lens modeling over different channel slices of the interferometric data using our lensing code UVMCMCFIT (Busmann et al. 2015; see Busmann et al. 2015 for details of the code). Models of each slice thus provide the properties on the intrinsic kinematics. To increase the SNR for modeling, the slices are obtained by binning five native channels ($\Delta v \sim 21.5 \text{ km s}^{-1}$) over the full linewidth of $\sim 750 \text{ km s}^{-1}$ in the original data, resulting in seven independent channels.

The lens mass distribution is modeled using a singular isothermal ellipsoid (SIE) profile, which is described by five free parameters: the positional offset in R.A. and Dec. relative to an arbitrary chosen fixed coordinate in the image, the Einstein Radius, the axial ratio, and the position angle. We use the VLA radio continuum emission toward the foreground galaxy to initialize the positional offset. We impose a uniform prior $\pm 0''.05$ in both $\Delta \text{R.A.}$ and $\Delta \text{Dec.}$, motivated by the astrometry uncertainties in the VLA image as well as the uncertainties provided by previous SIE lens model (C06). We initialize the Einstein Radius based on the model parameters reported by C06 and impose a uniform prior using $\pm 3\sigma$ of their uncertainties. The sources are modeled using elliptical Gaussian profiles, which are parameterized by six free parameters: the positional offset in R.A. and Dec. relative to the lens, the intrinsic flux density, the effective radius, the axial ratio, and the position angle. The position of each source is allowed to vary between $\pm 1''.5$ (i.e., within the Einstein Radius) and the effective radius is allowed to vary from $0''.01$ – $2''$.

Our code uses an Markov Chain Monte Carlo (MCMC) approach to sample the posterior probability distribution function (PDF). In each model, we require a target acceptance rate of ~ 0.25 – 0.5 and check for chain convergence by inspecting trace plots and requiring the samples are beyond at least an autocorrelation time. We thus employ $\sim 50,000$ samples as the initial “burn-in” phase to stabilize the Markov chains (which we then discard) and use the final $\sim 5,000$ steps, sampled by 128 walkers, to identify the posterior. Here, we identify the best-fit model and the quoted uncertainties using the median and the 68% confidence intervals in the marginal PDFs.

We first obtain a preliminary lens model for each channel slice independently, where their lens parameters are allowed to vary and are initialized according to the aforementioned way. We obtain the final model by repeating the modeling over each slice but fixing their lens parameters to the overall median in the preliminary models, as listed in Table 2. This ensures that all models share the same lens profile. The magnification factors in Table 3 are determined by taking the ratio between the image plane flux and the source plane flux of each model.

TABLE 2
LENS PARAMETERS CONSTRAINED BY
MODELS OF SEVEN VELOCITY CHANNELS

Parameters	Median values
Offset in RA (")	0.004 ± 0.027
Offset in Dec (")	0.003 ± 0.027
Axial Ratio	0.56 ± 0.16
Position Angle (deg)	103 ± 22
Einstein Radius (")	1.833 ± 0.002

NOTE. — Parameters describing the foreground lens are obtained based on the median in the preliminary models (see text for details). All angular offsets are with respect to $\alpha = 11^{\text{h}}31^{\text{m}}51^{\text{s}}.44$, $\delta = -12^{\circ}31'58''.3$ (J2000).

Our model parameters in Table 2, describing the mass distribution of the lensing galaxy, are consistent (within the uncertainties) with that of the SIE model presented by C06. We find a mass of $M(\theta < \theta_E) = (7.47 \pm 0.02) \times 10^{11} M_{\odot}$ within the Einstein radius.

5.1.1. Interpretation of the source-plane morphology

The reconstructed source locations in Figure 5 demonstrate an intrinsic velocity gradient across the source plane, which is indicative of a kinematically-ordered disk-like galaxy. Additional support to the disk conjecture can be found in the double-horned line profile (Figure 1) and the observed (image plane) velocity field (Figure 8). Furthermore, C06 also find that the reconstructed source plane emission in optical-NIR is best-reproduced using a $n=1$ Sersic profile. We thus interpret RXJ1131 to be a disk galaxy.

One other interesting result from our lens model is that a better fit is found for the red-most channel if we add a second source component (see top left panel in Figure 5). This is consistent with previous results reported by Brewer & Lewis (2008), who find an optically faint companion (component F in their paper) $\sim 2.4 \text{ kpc}$ away from the AGN host galaxy, and C06, who find evidence for an interacting galaxy near RXJ1131. Spatially, the red velocity component of the CO emission also coincides with this component F. It is therefore evident that we detect CO($J=2 \rightarrow 1$) emission in the companion galaxy. To quantify the type of merger (major v.s. minor) conventionally with a mass ratio, we decompose the total line flux into two components: one from RXJ1131 and the other from its companion. Since the companion is only detected in the red-most channel, we use the best-fit flux densities and magnification factors obtained from the model of this channel to derive the intrinsic gas mass in the companion. Without direct CO($J=1 \rightarrow 0$) measurements, we derive CO($J=1 \rightarrow 0$) intensity assuming a brightness temperature ratio of $r_{21} = 1$, which was chosen solely to facilitate a comparison with other U/LIRGs. For the same reason, we adopt a luminosity-to-mass conversion factor of $\alpha_{\text{CO}} = 0.8 \text{ (K km s}^{-1} \text{ pc}^2)^{-1}$. This yields a gas mass M_{gas} of $(1.92 \pm 0.09) \times 10^9 M_{\odot}$. For the molecular gas mass in RXJ1131, we derive its intrinsic line flux over the FWZI linewidth using the respective magnification factors listed in Table 3, which to first order takes

TABLE 3
MAGNIFICATION FACTORS OF VARIOUS KINEMATIC
COMPONENTS IN CO($J=2 \rightarrow 1$)

Velocity Range (km s ⁻¹)	Source 1 μ_L	Source 2 μ_L
-366 – -258	3.1 \pm 0.9	
-237 – -151	4.3 \pm 2.4	
-129 – -43	4.2 \pm 0.6	
-21.5 – 65	4.1 \pm 0.9	
86 – 172	8.7 \pm 2.0	
194 – 280	7.6 \pm 1.6	
301 – 388	7.2 \pm 5.6	6.7 \pm 2.5
weighted average	4.4	
median	5.5	

NOTE. — Velocity is taken from the center of each (native) channel without any binning. Each row corresponds to a channel slice used for lens modeling. Source 1 is RXJ1131 and source 2 is its companion. See text for details.

into account effect of differential lensing. This yields $I_{\text{CO}(J=2 \rightarrow 1)} = 2.93 \pm 0.70 \text{ Jy km s}^{-1}$, where the uncertainty includes those on the magnification factors. Adopting the same brightness temperature ratio and α_{CO} as used for the companion, this corresponds to a gas mass of $M_{\text{gas}} = (1.38 \pm 0.33) \times 10^{10} M_{\odot}$, implying a gas mass ratio of $\sim 7:1$ between RXJ1131 and its companion. We thus classify the system to be a “wet-wet” minor merger according to the classification scheme commonly used in literature.

The spatial resolution of the data in hand is a few arcsec, which implies that despite the high SNR and spectral resolution, this data is insufficient to constrain the intrinsic sizes of the lensed galaxies, and thus the magnification factors may be under-predicted.

5.1.2. Spatial extent and differential lensing

In the image plane shown in Figure 2, the redshifted component is cospatial with the Einstein Ring seen in the optical image, with most of its apparent flux originating from the lensed arc in the southeast, whereas the blue component is predominately coming from solely the lensed arc. To further illustrate this, we show the channel maps of 21.5 km s^{-1} width and a spatial spectra map of $1''.5$ resolution in Figure 6 and Figure 7, respectively. The figures show that emission is present to the west, peaking toward the lensing arc (black crosses in Figure 6) in the red wing, and shifts to the east with decreasing velocity (blue wing). This is consistent with the source plane positions in our models and is suggestive of an extended CO emitting region.

Similar to previous studies of RXJ1131, where differential lensing across *HST* V-, I-, and H-band has been detected with a magnification factor decreasing from 10.9 to 7.8 (C06), the highly asymmetric CO($J=2 \rightarrow 1$) line profile suggests that differential lensing is also non-negligible for CO, causing the redshifted emission to be apparently much brighter than the blueshifted component and the asymmetric line profile. To first order, this can be explained by the difference in magnification factor which varies from 8.7 to 3.1 across the CO($J=2 \rightarrow 1$) line (Table 3). Such an effect (difference in μ_L across channels)

is consistent with the source plane positions relative to the caustics in Figure 5, where the red wing emission mainly originates near the cusp of the caustic and the blue wing emission is located beyond the caustics. In fact, the intrinsic line flux of the redshifted and blueshifted emission in RXJ1131 (after subtracting a contribution from the companion) is $I_{\text{CO}(J=2 \rightarrow 1)} = 1.26 \pm 0.23 \text{ Jy km s}^{-1}$ and $1.25 \pm 0.23 \text{ Jy km s}^{-1}$, respectively, implying an intrinsically symmetric line profile. This is consistent with the source-plane velocity gradient in our lens model (see §5.1.1).

5.2. CO($J=2 \rightarrow 1$) Kinematics

A clear velocity gradient and a high velocity dispersion ($\gtrsim 400 \text{ km s}^{-1}$) near the central region is seen in Figure 8. While beam smearing is inevitably the dominant factor in the observed velocity dispersion at the spatial resolution of this data, the exceedingly high velocity dispersion may hint at potential perturbations from the AGN, or internal turbulence due to interactions with the companion, and/or instability due to the large gas content. Therefore, in this scenario, RXJ1131 is likely a disrupted disk galaxy hosting an optically bright quasar and is in the process of merging.

5.3. CO($J=2 \rightarrow 1$) Dynamical modeling

Assuming the velocities of the respective channels used in the lens modeling correspond to solely the tangential component of the true velocity vector of a rotating disk (i.e., along the major axis), we extract a one dimensional PV diagram in Figure 9 by slicing across their source plane positions (PA: 121°).

We then attempt to characterize the molecular gas kinematics using an empirically-motivated disk model (e.g., Courteau 1997; Puech et al. 2008; Miller et al. 2011):

$$V = V_0 + \frac{2}{\pi} V_a \arctan\left(\frac{R}{R_t}\right), \quad (1)$$

where V is the observed velocity, V_0 is the velocity at dynamical center, V_a is the asymptotic velocity, and R_t is the “turnover” radius at which the rotation curve becomes flat. We perform non-linear least square fitting using an orthogonal distance regression to find the best-fit parameters, taking into account the uncertainties in both velocity (channel width) and distance offset. We also place an upper limit on $R_t < 15 \text{ kpc}$ to keep this parameter physical (e.g., Puech et al. 2008; Miller et al. 2011). The parameter uncertainties are inferred based on Monte Carlo simulation of 500 iterations, where the input parameters are perturbed according to random Gaussian distributions of sigmas corresponding to their uncertainties. Using this model, we find $V_a = 975 \pm 387 \text{ km s}^{-1}$, $R_t = 10.7 \pm 5.7 \text{ kpc}$, and $V_0 = 28 \pm 40 \text{ km s}^{-1}$. However, since emission is not resolved along the flat regime of the rotation curve, the asymptotic velocity is poorly constrained and the “turnover” radius is at most a lower limit. In particular, V_a and R_t are highly correlated with a Pearson coefficient $R = 0.998$, and 0.027 between V_a and V_0 .

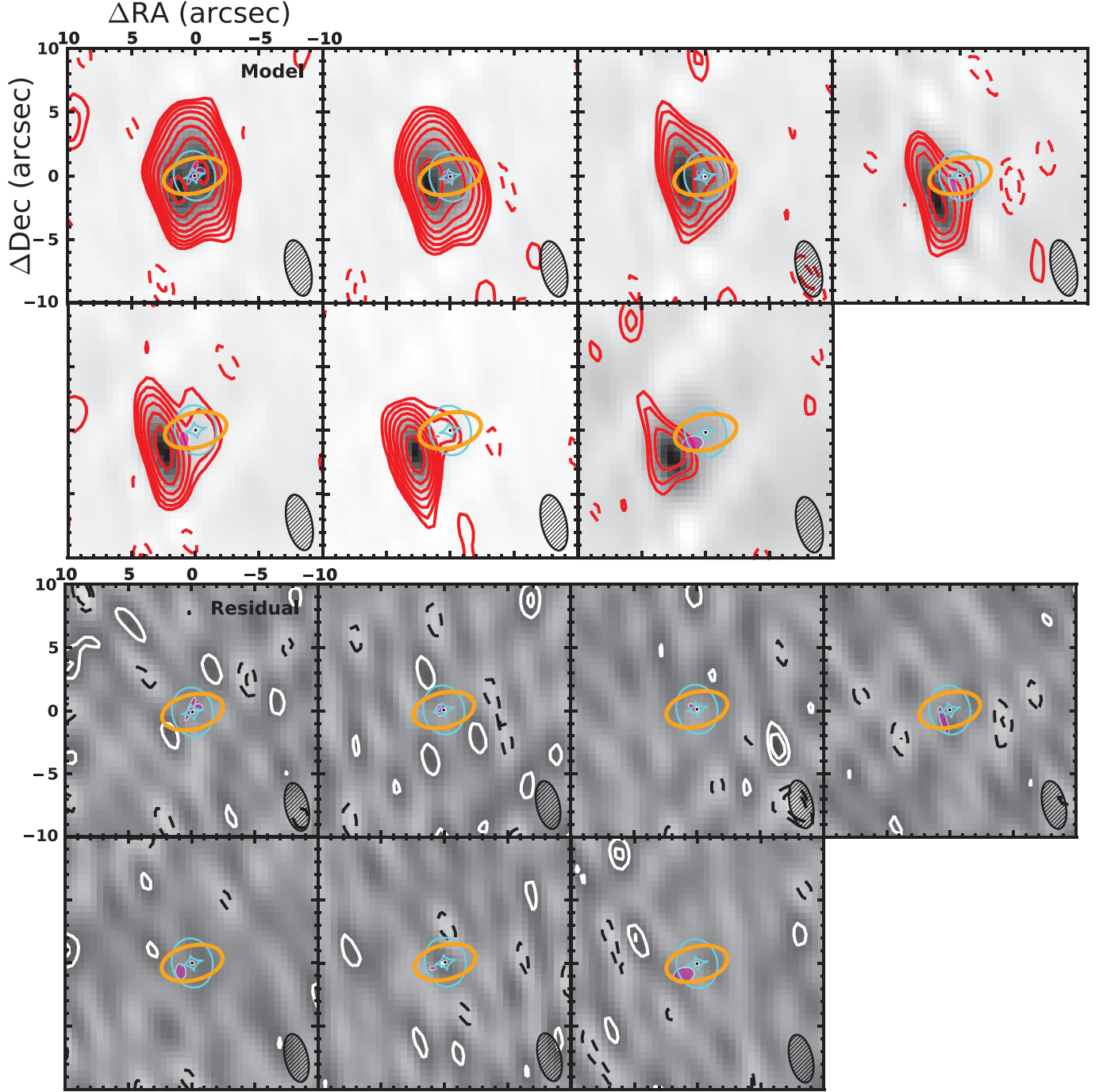


FIG. 5.— Each panel corresponds to a lens model of RXJ1131 performed over a channel slice $\sim 100 \text{ km s}^{-1}$ of the $\text{CO}(J=2 \rightarrow 1)$ data. Top: channel maps of the PdBI $\text{CO}(J=2 \rightarrow 1)$ emission (red) overlaid on our best-fit lens models (grayscale). The location of the foreground lensing galaxy is indicated by a black dot and its critical curve is traced by the orange solid line. The locations and morphologies (half-light radii) of the reconstructed sources are represented by magenta ellipses. The caustic curves are represented as cyan lines. The beam of the PdBI observations is shown in the bottom right corner of each panel. Bottom: residual images of the best-fit models, obtained by taking the Fourier transform after subtracting the best-fit model from the data in the uv -domain. Contours start at $\pm 3\sigma$ and increment at steps of $3 \times 2^n \sigma$, where n is a positive integer.

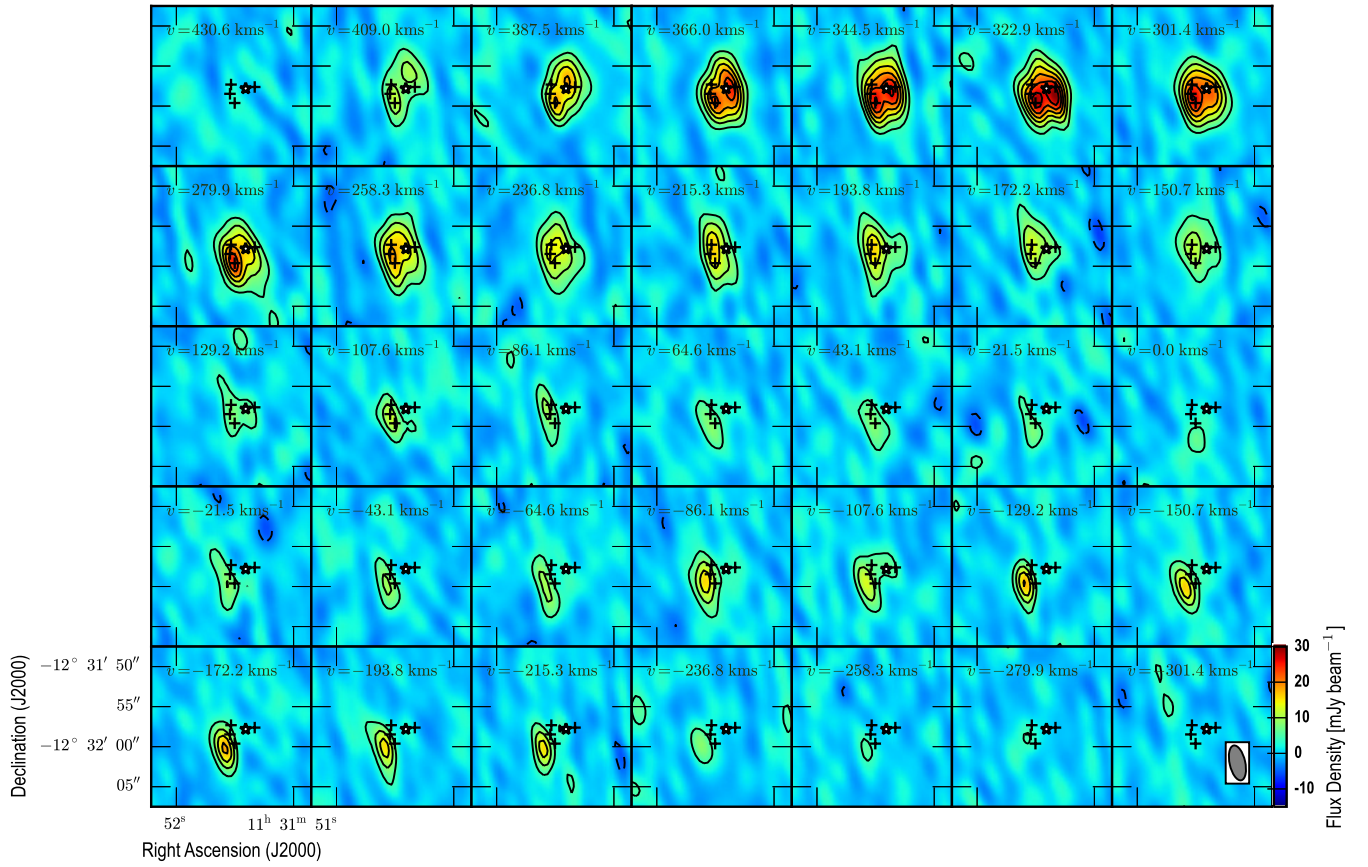


FIG. 6.— Channel maps of PdBI CO($J=2 \rightarrow 1$) toward RXJ1131 in 21.5 km s^{-1} resolution. Black crosses indicate the position of the lensed knots (AGN emission, which correspond to components ABCD in C06). The central white-filled star indicates the position of the foreground lensing galaxy (component G in C06). Contours start and increment at steps of $\pm 3\sigma$. The beam is denoted in the bottom right panel.

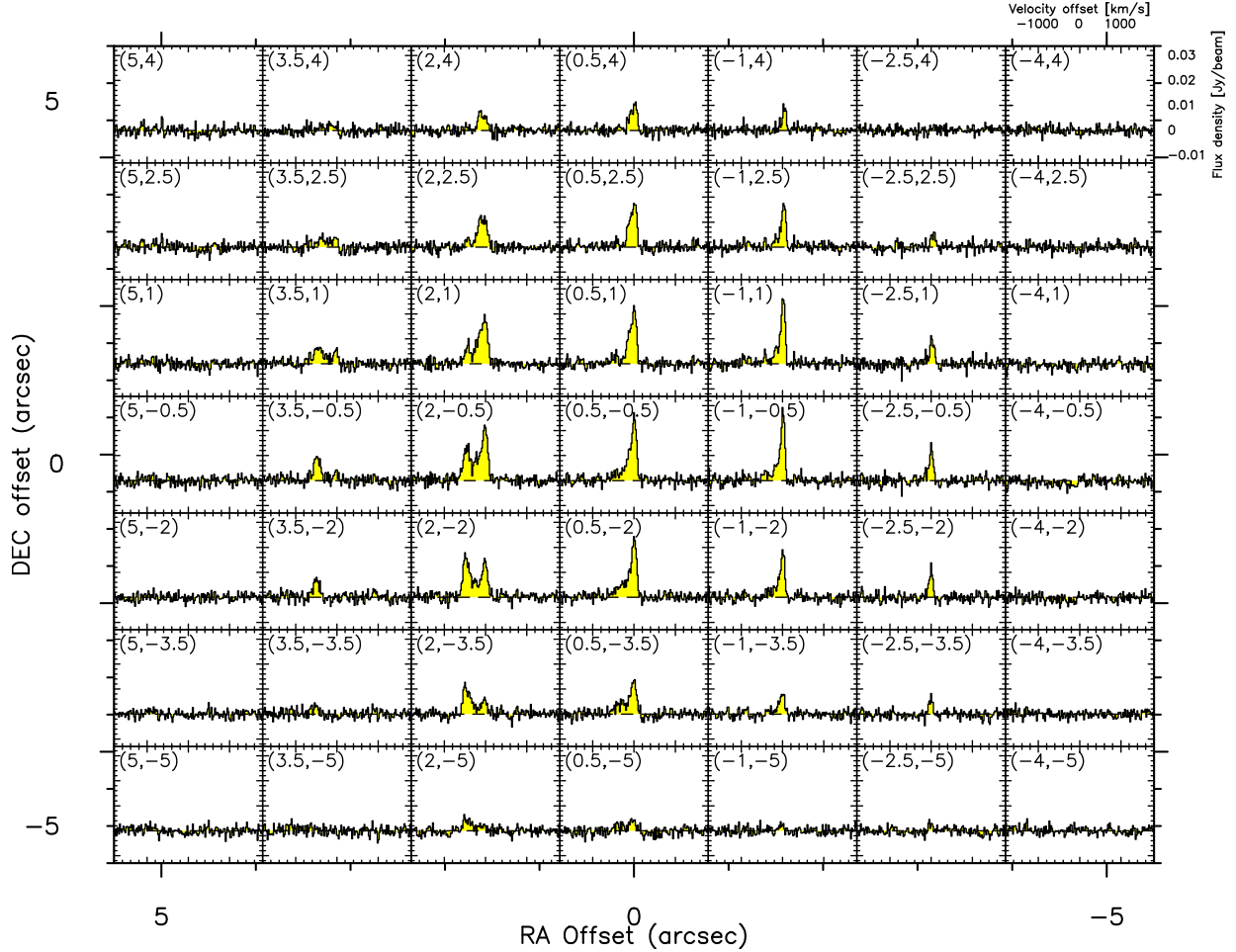


FIG. 7.— CO($J=2 \rightarrow 1$) spectrum as a function of position, binned by 3 pixels in each direction ($1''.5$). The spectra map covers an extent of $\sim 10'' \times 10''$ centering on the pixel that corresponds to the lensing galaxy. Spatial offset in arcsec is denoted in top left corner of each panel. The velocity and flux density scales are denoted in the top right panel.

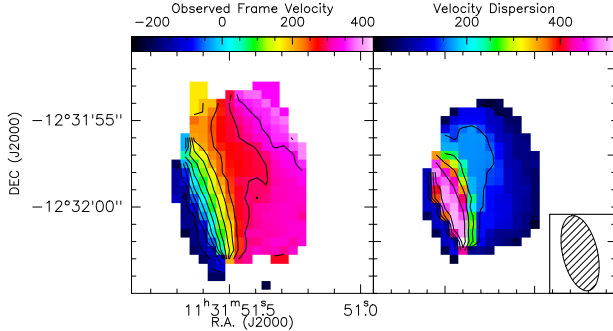


FIG. 8.— Contours for the first (left) and second (right) moment maps are shown in steps of 50 km s^{-1} , and 100 km s^{-1} , respectively. The beam (native resolution) is shown in the right panel.

The asymptotic velocity (V_a) – an extrapolation of the model out to radius beyond the disk scale-length and half-light radius – is not equivalent to maximum observed velocity (V_{max}), which is commonly used in literature to parameterize disc rotation. The arctangent model is most commonly used in studies of the Tully-Fisher relation, where an extrapolation to $V_{2.2}$ (velocity at 2.2 disc scale-length or ~ 1.375 half-light radius, or $\sim 0.7R_{\text{opt}}^4$) is typ-

⁴ Radius enclosing 83% of the light distribution.

ically adopted as the rotation velocity (V_{max} in their terminology) since this corresponds to the radius at which the velocity of a pure exponential disk peaks (Courteau & Rix 1997). We here adopt the maximum *observed* velocity $V_{\text{rot}} = 345 \pm 55 \text{ km s}^{-1}$ at $6 \pm 3 \text{ kpc}$ from the dynamical center as a proxy to the rotation velocity. This radius corresponds to $\sim 0.6R_e$, where R_e is the half-light radius $\sim 10.3 \text{ kpc}$ inferred from the *HST* *I*-band lens model (C06; converted to our cosmology). We note that the source plane half-light radius varies substantially with wavelength. In particular, the half-light radius is found to be $\sim 4 \text{ kpc}$ and $\sim 7 \text{ kpc}$ in *V*-band (Brewer & Lewis 2008) and *H*-band (C06), respectively. The CO gas is thus of similar spatial extent as *H* and *I*-bands.

In the rest-frame, emission in the observed *H*-band corresponds to NIR emission, tracing radiation from the accretion disk surrounding the central AGN and also from old and evolved stellar populations; *I*-band corresponds to roughly the optical *V*-band, tracing stellar radiation from existing, less massive (i.e., longer-lasting) stars; *V*-band corresponds to roughly *U*-band, tracing radiation from massive young stars in the host galaxy. Hence, the *V*-band compactness may be explained in part due to the fact that its emission is more susceptible to dust extinction than

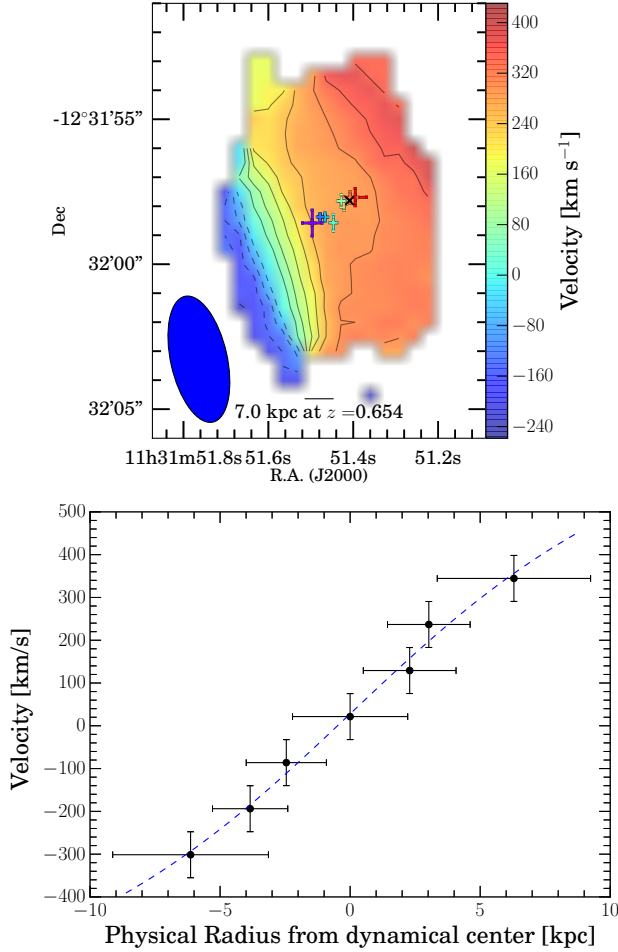


FIG. 9.— Top: Source-plane positions from best-fit CO($J=2 \rightarrow 1$) lens models are indicated with their associated uncertainties atop the observed first moment map. The contours are at steps of 50 km s^{-1} . Bottom: PV slice along the major axis in the source plane at $\text{PA} = 121^\circ$. Dashed line shows the best-fit rotation curve using an arctangent model. The vertical error bars show the channel width for each model and the horizontal error bars are the 1σ uncertainties on the source plane positions.

in other bands and/or a central starburst caused by higher concentrations of star-forming gas towards the central regions – owing to gravitational perturbations induced from interactions with the companion (e.g., Di Matteo et al. 2005). The rest-frame NIR emission is likely to be dominated by evolved stars since the AGN is located at $\sim 0''.016$ inside the central region of the host galaxy (Sluse et al. 2006), implying a compact accretion disk. This is consistent with the picture that old stars form first and constitute the bulge component of a spiral galaxy and that nuclear starbursts are triggered in mergers.

Using V_{rot} estimate from the modeling, we find a dynamical mass of $M_{\text{dyn}} \sin^2 i (< 6 \text{ kpc}) = 17 \times 10^{10} M_\odot$ enclosed within the CO-emitting region. If we instead consider the CO($J=2 \rightarrow 1$) line peak separation ($\Delta v_{\text{sep}}/2 \sim 200 \text{ km s}^{-1}$) as the rotation velocity, we find $M_{\text{dyn}} \sin^2 i (< 6 \text{ kpc}) = 5.8 \times 10^{10} M_\odot$. We correct for the inclination effect using the morphological axial ratio ($a/b \sim 1''.8 / 3''.25$) from the reconstructed image (Figure 3 in C06), yielding an inclination angle of 56.4° , which is consistent with the observed unobscured AGN and an observable double peak

TABLE 4
SED FITTING RESULTS

Parameters	With $24\mu\text{m}$	Without $24\mu\text{m}$
T_d (K)	$52.0^{+4.0}_{-4.1}$	$58.2^{+14.5}_{-14.4}$
β	$1.8^{+0.5}_{-0.6}$	$2.1^{+0.3}_{-0.3}$
α	$1.6^{+0.5}_{-0.5}$	$8.9^{+6.9}_{-6.3}$
λ_0^a (μm)	548^{+285}_{-307}	367^{+125}_{-145}
λ_{peak}^b (μm)	162^{+16}_{-30}	146^{+39}_{-44}
$f_{\text{norm}, 500\mu\text{m}}^c$ (mJy)	59^{+14}_{-13}	60^{+5}_{-5}
L_{FIR}^d ($10^{12} L_\odot$)	$3.81^{+2.04}_{-1.92}$	$4.72^{+2.54}_{-2.26}$
M_d^e ($10^8 M_\odot$)	22^{+5}_{-18}	11^{+5}_{-6}

NOTE. — Errors reported here are $\pm 1\sigma$. L_{FIR} and M_d are not corrected for lensing.

^a Observed-frame wavelength where $\tau_\nu = 1$

^b Observed-frame wavelength of the SED peak

^c Observed-frame flux density at $500 \mu\text{m}$

^d Rest-frame $42.5\text{--}122.5 \mu\text{m}$ luminosity

^e Derived assuming absorption mass coefficient of $\kappa = 2.64 \text{ m}^2 \text{ kg}^{-1}$ at $\lambda = 125.0 \mu\text{m}$ (Dunne et al. 2003)

line profile. The dynamical mass is then $8.3 \times 10^{10} M_\odot < M_{\text{dyn}} (< 6 \text{ kpc}) < 25 \times 10^{10} M_\odot$. Since this quantity is derived under the assumption that the gas is virialized, which is highly unlikely given the velocity dispersion and the presence of a close companion, our estimate is at most an upper limit.

5.4. SED modeling

We fit dust SED models to the $24 \mu\text{m}$ – 2.2 mm photometry in Figure 10, where we also include the IRAS $60 \mu\text{m}$ and $100 \mu\text{m}$ upper limits to constrain the dust peak. The fit is performed with the code MBB_EMCEE (e.g., Riechers et al. 2013; Dowell et al. 2014), which samples the posterior using an MCMC approach and uses instrumental response curves to perform color correction on-the-fly. The SED model consists of a modified-blackbody function with a power-law attached to the Wien side to account for an excess in the MIR owing to warm, small dust emission. The model is thus described by five free parameters: the rest-frame characteristic dust temperature (T_d), the emissivity index (β), the power-law index (α), the flux normalization at $500 \mu\text{m}$ (f_{norm}), and the observed-frame wavelength at which the emission becomes optically thick (λ_0). We impose an upper limit of 100 K on T_d (commonly BLAH in ULIRGs; CITE), a Gaussian prior centered around $\mu = 1.9$ with $\sigma = 0.3$ on β , and an upper limit of $1000 \mu\text{m}$ on λ_0 . We check for chain convergence by requiring the autocorrelation length of each parameter to be less than the number of steps taken for the burn-in phase (which are then discarded). Here we report the means and the 1σ confidence interval in the marginal PDFs as the best-fit parameters, as listed in Table 4.

In the first model, we include the $24 \mu\text{m}$ data to constrain the power-law index. Based on the best-fit of this model, we find a far-IR luminosity (rest-frame $42.5\text{--}122.5 \mu\text{m}$) of $3.81^{+2.04}_{-1.92} \times 10^{12} L_\odot$ and a dust mass of $22^{+5}_{-18} \times 10^8 M_\odot$, uncorrected for lensing. For the mass absorption coefficient, we adopt $\kappa = 2.64 \text{ m}^2 \text{ kg}^{-1}$ at $125.0 \mu\text{m}$ (rest frame; Dunne et al. 2003). The dust mass uncertainty does not

include those in the absorption coefficient.

A fit including the MIR $24\ \mu\text{m}$ photometry is likely an upper limit on the far-IR luminosity arising from the starburst in the AGN host galaxy. If we instead fit for a model excluding the $24\ \mu\text{m}$ constraint, two major consequences are immediately apparent. First, the power-law index is poorly-constrained (see Table 4). Second, the steep power-law implies a small contribution from the power-law regime to the total IR luminosity as compared to the graybody. Thus, the far-IR luminosity in this model should, in principle, correspond to a lower limit on the cold dust emission. Using the best-fit parameters for this model, we find a total IR luminosity L_{IR} (rest-frame $8-1000\ \mu\text{m}$) of $9.71^{+6.14}_{-6.05} \times 10^{12} L_{\odot}$, a far-IR luminosity L_{FIR} of $4.72^{+2.54}_{-2.26} \times 10^{12} L_{\odot}$ and a dust mass M_{dust} of $11^{+5}_{-6} \times 10^8 M_{\odot}$, uncorrected for lensing. Taken at face value, this implies a FIR-to-IR luminosity ratio of $\sim 58 \pm 35\%$.

The dust temperature from both models is similar to that of ULIRGs at $0.6 < z < 1.0$ ($54 \pm 5\ \text{K}$; Combes et al. 2013, hereafter C13). We note the far-IR luminosity is comparable in both models, which is not surprising given the lack of constraints in the MIR. For the subsequent analysis, we adopt the physical quantities from the first model (i.e., with constraints at $24\ \mu\text{m}$). The choice of SED model does not affect the derived star formation rate (SFR) given the similar far-IR luminosity. Yet, the dust mass is higher in the former but consistent within the uncertainties. We correct for lensing using the median magnification factor ($\mu_L = 5.5$) from the CO lens models. This yields a L_{FIR} of $(6.9 \pm 3.6) \times 10^{11} L_{\odot}$ and a total IR luminosity of $\sim 1.5 \times 10^{12} L_{\odot}$, implying RXJ1131 is a ULIRG. Assuming a Salpeter initial mass function (Salpeter 1955), we find a SFR_{FIR} of $(120 \pm 63) M_{\odot}\ \text{yr}^{-1}$ using the standard conversion (Kennicutt 1998).

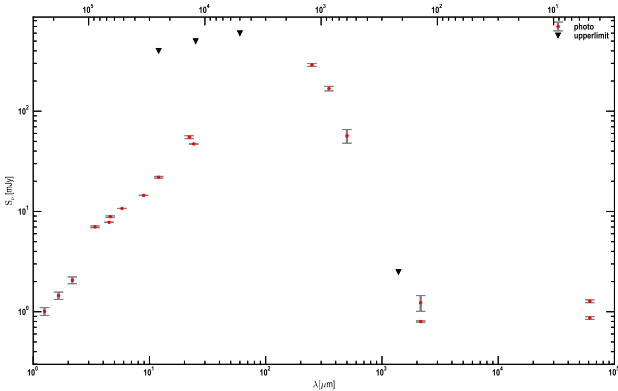


FIG. 10.— SED models of the IR dust emission toward RXJ1131. **This figure needs an update** WISE flux is slightly higher than the IRAC point, probably due to a smaller aperture used in IRAC extraction, both of which were taken from the archive. IRAC: Aperture flux in $5''$ diameter. MIPS: use PSF fit flux from archive as source size $< \text{PSF FWHM}$ of $6''$. Might want to add NVSS constraints.

5.5. Gas properties

In this section, we derive the gas properties of the merger based on $\text{CO}(J=2 \rightarrow 1)$ and compare with those reported

by C13, which is the largest sample of IR-luminous galaxy at similar redshift ($0.6 < z < 1.0$) with CO measurements⁵. We note their results are based on $\text{CO}(J=2 \rightarrow 1)$ and $\text{CO}(J=4 \rightarrow 3)$ line observations on the single-dish IRAM 30-m.

5.5.1. Linewidth & Sizes

We find that the linewidths for both components (redshifted and blueshifted) inferred from a double Gaussian fit to the line profile are comparable to the C13 ULIRG sample (Δv_{FWHM} of $370\ \text{km s}^{-1}$) and local ULIRGs ($300 \pm 85\ \text{km s}^{-1}$; Solomon et al. 1997). Since C13 do not have resolved observations, we compare the gas distribution with local U/LIRGs. The CO gas in RXJ1131 is distributed $\sim 6\ \text{kpc}$ in radius across (in the source plane), which is more extended than the sample of disk-like U/LIRGs studied by Ueda et al. (2014, hereafter U14), who find an average radius of $3.5 \pm 2.3\ \text{kpc}$ with a range spanning $1.1 - 9.3\ \text{kpc}$.

5.5.2. Gas Mass

To derive the molecular gas mass, we first correct for lensing magnification using the respective magnification factors listed in Table 3, which to first order takes into account effect of differential lensing. This yields $I_{\text{CO}(J=2 \rightarrow 1)} = 5.9 \pm 2.7\ \text{Jy km s}^{-1}$, where the uncertainty includes those on the magnification factors.

Without direct $\text{CO}(J=1 \rightarrow 0)$ measurements, we derive $\text{CO}(J=1 \rightarrow 0)$ intensity using a brightness temperature ratio of $r_{32} = 1$, which was chosen solely to facilitate a comparison with other U/LIRGs. For the same reason, we adopt a luminosity-to-mass conversion factor of $\alpha_{\text{CO}} = 0.8\ (\text{K km s}^{-1}\ \text{pc}^2)^{-1}$, this yields a CO luminosity $L'_{\text{CO}} = (3.47 \pm 1.58) \times 10^{10}\ \text{K km s}^{-1}\ \text{pc}^2$ and a gas mass M_{gas} of $(xx \pm xx) \times 10^{10} M_{\odot}$. BLAH The inferred gas mass is comparable to C13 sample ($M_{\text{gas}} = 1.5 \times 10^{10} M_{\odot}$) as well as local U/LIRGs (Solomon et al. 1997; Sanders & Mirabel 1996) but higher than local LIRGs (U14).

We place a lower limit on the dynamical mass (see §5.3) using the inferred gas mass. This BLAH. **will need edit depending on the dyn. modeling section** a gas-to-dynamical mass fraction of $f_{\text{gas-dyn}} = \text{BLAH}$. Using the dust mass derived from SED fitting, we find a gas-to-dust ratio of 184 ± 124 , which is consistent with the C13 sample ($f_{\text{gas-dust}} = 206$) and local U/LIRGs (200–350; Sanders et al. 1991, Contini & Contini 2003; Seaquist et al. 2004; Wilson et al. 2008).

5.5.3. SFE and Depletion Time

We derive the SFE using the far-IR luminosity definition used by C13 (i.e., $\text{SFE} \pm L_{\text{FIR}} (40-500\ \mu\text{m}) / M_{\text{gas}}$), we find a SFE of 31 ± 15 for RXJ1131, or equivalently a depletion timescale of $\tau = 190 \pm 70\ \text{Myr}$. This SFE is substantially lower than most U/LIRGs (Solomon et al. 1997; Combes et al. 2011; C13).

⁵ The far-IR luminosity in C13 is derived based on $60\ \mu\text{m}$ and $100\ \mu\text{m}$ IRAS fluxes, and using a different definition of L_{FIR} : rest-frame $40-500\ \mu\text{m}$. Following this convention, we find a far-IR luminosity of $L_{\text{FIR}} = (8.8 \pm 0.4) \times 10^{11} (\mu_L/5.5)^{-1} L_{\odot}$ and a SFR of $(150 \pm 70) M_{\odot}\ \text{yr}^{-1}$.

Implication of this unexpectedly low SFE in RXJ1131...

6. DISCUSSION

6.1. Merger stage of RXJ1131-1231

In this section, we put our results in context with other ULIRGs/mergers at $z=0-1$. It is clear that RXJ1131 has a gas-rich companion, but how does this affect its internal dynamics? What is the merger stage of RXJ1131? We argued that the symmetric source-plane velocity field suggest the system is a minor merger, consistent with an earlier study by B08, who independently conclude that the companion is likely a dwarf of size ~ 700 kpc across.

While our result is consistent with other studies of RXJ1131, it contrast strongly with studies of local (U)LIRGs/mergers ($L_{\text{IR}} = 10^{11-12.5} L_{\odot}$; $z < 0.1$), where AGNs are typically found in late stage mergers (Yuan et al. 2010; Iwasawa et al. 2011; Carpineti et al. 2012) and that only these major mergers near their final coalescence can provide $L_{\text{IR}} > 10^{12} L_{\odot}$, (e.g., Carpineti et al. 2015; Larson et al. 2016, hereafter L16)⁶. If this is also the case at $z \sim 0.65$, it would imply RXJ1131 is a major merger near its final coalescence and that the spatially offset component is likely an expulsion of gas driven by AGN winds or some tidally ejected material from previous passage. In that case, the molecular gas fraction in the host galaxy should have declined (as seen in ellipticals) compared to early stage mergers **can we find molecular gas mass fraction as a function of merger stage? also, what is the dynamical mass for RXJ1131** and that the molecular gas would be more concentrated in the nuclear region. This is inconsistent with what is observed for RXJ1131 (an extended gas-rich disk; but see also U14 for outliers with extended molecular gas in merger remnants) and the fact that there is on-going star formation activity. Hence, we reject this and speculate the discrepancy is a consequence of different power mechanisms of IR-luminous galaxies at intermediate redshift.

— **anything below is not ready** —

6.1.1. Fate of RXJ1131-1231

Has RXJ1131 encountered with the companion?

From numerical simulations, mergers are observable and distinguishable with their kinematic and morphological features for 0.2–0.4 Gyr between their second passage and final coalescence.

The spinning black hole in RXJ1131 provide one piece of evidence that the two has already encountered.

Mergers are expected to evolve into local ellipticals or large-disks (bulge dominated) (springel & Hernquist 05, cite). Given the extended molecular gas distribution, we suggest RXJ1131 may evolve into the latter (large-disk) unless the “companion” BKAH SOME STUFF or some other mechanisms at play in the latter stage, transporting the gas toward the central nuclear region and blah.

6.2. ULIRG Evolution and Cosmic SFH

⁶ In this section, we adopt the total IR luminosity calculated from 8–1000 μm to be consistent with the classification used by these authors.

While there is an emerging consensus on the strong evolution of the IR luminosity function (e.g., Huynh et al. 2007; Seymour et al. 2010), it is currently unclear whether the IR luminosity of these intermediate redshift sources arise due to the merging of large spiral galaxies, as typically seen in local ULIRGs, or proceed under a different formation processes at higher redshifts. Our study blah...

Our result indicates that...

7. SUMMARY AND CONCLUSIONS

We investigate the cold gas kinematics and dynamics in the lensed optical quasar RXJ1131 at $z_{\text{CO}} \sim 0.65$ by observing its CO($J=2 \rightarrow 1$) and CO($J=3 \rightarrow 2$) line emission. Our results suggest that RXJ1131 is a wet-wet merger between an AGN/starburst ULIRG and a optically faint companion.

This work is based on observations carried out under project number S14BX001 with the IRAM NOEMA Interferometer. IRAM is supported by INSU/CNRS (France), MPG (Germany) and IGN (Spain). Support for CARMA construction was derived from the Gordon and Betty Moore Foundation, the Kenneth T. and Eileen L. Norris Foundation, the James S. McDonnell Foundation, the Associates of the California Institute of Technology, the University of Chicago, the states of Illinois, California, and Maryland, and the National Science Foundation. Ongoing CARMA development and operations are supported by the National Science Foundation under a cooperative agreement and by the CARMA consortium universities. The National Radio Astronomy Observatory is a facility of the National Science Foundation operated under cooperative agreement by Associated Universities, Inc. This research made use of data obtained with *Herschel*, an ESA space observatory with science instruments provided by European-led Principal Investigator consortia and with important participation from NASA. This research has made use of NASA’s Astrophysics Data System Bibliographic Services. This work is based in part on observations made with the *Spitzer Space Telescope*, which is operated by the Jet Propulsion Laboratory, California Institute of Technology under a contract with NASA. This publication made use of data products from the Wide-field Infrared Survey Explorer, which is a joint project of the University of California, Los Angeles, and the Jet Propulsion Laboratory/California Institute of Technology, funded by the National Aeronautics and Space Administration. This publication made use of data products from the Two Micron All Sky Survey, which is a joint project of the University of Massachusetts and the Infrared Processing and Analysis Center/California Institute of Technology, funded by the National Aeronautics and Space Administration and the National Science Foundation. This research made use of the NASA/IPAC Extragalactic Database (NED) which is operated by the Jet Propulsion Laboratory, California Institute of Technology, under contract with the National Aeronautics and Space Administration. This research made use of Astropy, a community-developed core Python package for Astron-

omy (Astropy Collaboration et al. 2013). This research made use of APLpy, an open-source plotting package for Python hosted at <http://aplpy.github.com>.

Facilities: IRAM PdBI, CARMA, VLA, Herschel (SPIRE), WISE, IRAS, 2MASS, Spitzer (IRAC, MIPS), HST (ACS, NICMOS)

Astropy Collaboration, Robitaille, T. P., Tollerud, E. J., et al. 2013, *A&A*, **558**, A33
 Brewer, B. J., & Lewis, G. F. 2008, *MNRAS*, **390**, 39
 Busmann, R. S., Riechers, D., Fialkov, A., et al. 2015, *ApJ*, **812**, 43
 Busmann, S., Leung, T. K. D., & Conley, A. 2015, *uvcmcf*
 Calzetti, D. 2001, *PASP*, **113**, 1449
 Carpineti, A., Kaviraj, S., Darg, D., et al. 2012, *MNRAS*, **420**, 2139
 Carpineti, A., Kaviraj, S., Hyde, A. K., et al. 2015, *A&A*, **577**, A119
 Combes, F., García-Burillo, S., Braine, J., et al. 2011, *A&A*, **528**, A124
 —. 2013, *A&A*, **550**, A41
 Courteau, S. 1997, *AJ*, **114**, 2402
 Courteau, S., & Rix, H.-W. 1997, in *Bulletin of the American Astronomical Society*, Vol. 29, American Astronomical Society Meeting Abstracts, 1332
 Di Matteo, T., Springel, V., & Hernquist, L. 2005, *Nature*, **433**, 604
 Dowell, C. D., Conley, A., Glenn, J., et al. 2014, *ApJ*, **780**, 75
 Dunne, L., Eales, S. A., & Edmunds, M. G. 2003, *MNRAS*, **341**, 589
 Fazio, G. G., Hora, J. L., Allen, L. E., et al. 2004, *ApJS*, **154**, 10
 Hinshaw, G., Larson, D., Komatsu, E., et al. 2013, *ApJS*, **208**, 19
 Huynh, M. T., Frayer, D. T., Mobasher, B., et al. 2007, *ApJ*, **667**, L9
 Iwasawa, K., Sanders, D. B., Teng, S. H., et al. 2011, *A&A*, **529**, A106
 Kennicutt, Jr., R. C. 1998, *ARA&A*, **36**, 189
 Larson, K. L., Sanders, D. B., Barnes, J. E., et al. 2016, *ArXiv e-prints*, [arXiv:1605.05417](https://arxiv.org/abs/1605.05417)
 Miller, S. H., Bundy, K., Sullivan, M., Ellis, R. S., & Treu, T. 2011, *ApJ*, **741**, 115

Neugebauer, G., Habing, H. J., van Duinen, R., et al. 1984, *ApJ*, **278**, L1
 Ott, S. 2010, in *Astronomical Society of the Pacific Conference Series*, Vol. 434, *Astronomical Data Analysis Software and Systems XIX*, ed. Y. Mizumoto, K.-I. Morita, & M. Ohishi, 139
 Puech, M., Flores, H., Hammer, F., et al. 2008, *A&A*, **484**, 173
 Reis, R. C., Reynolds, M. T., Miller, J. M., & Walton, D. J. 2014, *Nature*, **507**, 207
 Riechers, D. A., Bradford, C. M., Clements, D. L., et al. 2013, *Nature*, **496**, 329
 Rieke, G. H., Young, E. T., Engelbracht, C. W., et al. 2004, *ApJS*, **154**, 25
 Salpeter, E. E. 1955, *ApJ*, **121**, 161
 Sanders, D. B., & Mirabel, I. F. 1996, *ARA&A*, **34**, 749
 Sanders, D. B., Scoville, N. Z., & Soifer, B. T. 1991, *ApJ*, **370**, 158
 Seymour, N., Symeonidis, M., Page, M. J., et al. 2010, *MNRAS*, **402**, 2666
 Skrutskie, M. F., Cutri, R. M., Stiening, R., et al. 2006, *AJ*, **131**, 1163
 Sluse, D., Surdej, J., Claeskens, J.-F., et al. 2003, *A&A*, **406**, L43
 Sluse, D., Claeskens, J.-F., Altieri, B., et al. 2006, *A&A*, **449**, 539
 Solomon, P. M., Downes, D., Radford, S. J. E., & Barrett, J. W. 1997, *ApJ*, **478**, 144
 Stern, D., Eisenhardt, P., Gorjian, V., et al. 2005, *ApJ*, **631**, 163
 Ueda, J., Iono, D., Yun, M. S., et al. 2014, *ApJS*, **214**, 1
 Wright, E. L., Eisenhardt, P. R. M., Mainzer, A. K., et al. 2010, *AJ*, **140**, 1868
 Yuan, T.-T., Kewley, L. J., & Sanders, D. B. 2010, *ApJ*, **709**, 884